The interplay of self-interacting dark matter and baryons in shaping the halo evolution

Giulia Despali [1]★ Martin Sparre [2,3,4] Simona Vegetti,[1] Mark Vogelsberger,[4] Jesús Zavala[5] and Federico Marinacci [4,6]

[1]*Max Planck Institute for Astrophysics, Karl-Schwarzschild-Strasse 1, D-85748 Garching bei München, Germany*
[2]*Institut fur Physik und Astronomie, Universität Potsdam, Karl-Liebknecht-Str 24/25, D-14476 Golm, Germany*
[3]*Leibniz-Institut fur Astrophysik Potsdam (AIP), An der Sternwarte 16, D-14482 Potsdam, Germany*
[4]*Department of Physics, Kavli Institute for Astrophysics and Space Research, Massachusetts Institute of Technology, Cambridge, MA 02139, USA*
[5]*Center for Astrophysics and Cosmology, Science Institute, University of Iceland, Dunhagi 5, 107 Reykjavik, Iceland*
[6]*Institute for Theory and Computation, Harvard-Smithsonian Center for Astrophysics, 60 Garden Street, Cambridge, MA 02138, USA*

ABSTRACT

We use high-resolution hydrodynamical simulation to test the difference of halo properties in cold dark matter (CDM) and a self-interacting dark matter (SIDM) scenario with a constant cross-section of $\sigma^T/m_\chi = 1\,\mathrm{cm}^2\,\mathrm{g}^{-1}$. We find that the interplay between dark matter self-interaction and baryonic physics induces a complex evolution of the halo properties, which depends on the halo mass and morphological type, as well as on the halo mass accretion history. While high-mass haloes, selected as analogues of early-type galaxies, show cored profiles in the SIDM run, systems of intermediate mass and with a significant disc component can develop a profile that is similar or cuspier than in CDM. The final properties of SIDM haloes – measured at $z = 0.2$ – correlate with the halo concentration and formation time, suggesting that the differences between different systems are due to the fact that we are observing the impact of self-interaction. We also search for signatures of SIDM in the lensing signal of the main haloes and find hints of potential differences in the distribution of Einstein radii, which suggests that future wide-field survey might be able to distinguish between CDM and SIDM models on this basis. Finally, we find that the subhalo abundances are not altered in the adopted SIDM model with respect to CDM.

Key words: gravitational lensing: strong – methods: numerical – galaxies: haloes – dark matter.

1 INTRODUCTION

One of the most important and long-lasting challenges of modern astrophysics is understanding and unveiling the nature of dark matter. Despite the many uncertainties on its composition, dark matter is considered the main driver of large-scale structure formation in the Universe. Moreover, the Λ Cold Dark Matter (ΛCDM) model has been successful in explaining many aspects of galaxy formation and evolution, as well as in reproducing the density fluctuations in the early Universe with great accuracy (e.g. Planck Collaboration et al. 2014). On the other hand, *N*-body simulations based on cold dark matter (CDM) models present some discrepancies with observed quantities, such as the 'missing satellites', the 'too-big-to-fail', and the 'core-cusp' problems (Klypin et al. 1999; Boylan-Kolchin et al. 2009; Bullock & Boylan-Kolchin 2017).

Alternative models such as warm dark matter (WDM) or self-interacting dark matter (SIDM) have been proposed to solve these controversies. The main feature of WDM is the suppression in the abundance of small mass structures (Schneider 1992; Lovell et al. 2012, 2014) and for this reason, it has been advocated as a solution in particular to the 'missing satellites' problem (Lovell et al. 2017). On the other hand, even if the central densities of haloes are reduced in WDM, leading to a different concentration–mass relation (Ludlow et al. 2016), viable WDM models do not significantly alter the inner structure of haloes. The original motivation to explore dark matter self-interaction was the fact that it is another possible source of suppression of low-mass (sub)haloes. However, the cross-section required for this to happen in (at least dark-matter-only) simulations is too large ($\simeq 10\,\mathrm{cm}^2\,\mathrm{g}^{-1}$), above the most recent constraints (Peter et al. 2013; Zavala, Vogelsberger & Walker 2013). At the same time, one of the main signatures of SIDM lies in the creation of cores in the density profiles: these are generated by energy-exchange interactions, due to which the halo centre is heated and

tends to become isothermal. The extent of the core and the central density depend on the SIDM cross-section: larger cross-sections produce larger cores (Yoshida et al. 2000; Davé et al. 2001; Colín et al. 2002; Vogelsberger, Zavala & Loeb 2012; Rocha et al. 2013; Vogelsberger et al. 2014b, 2016). If the self-scattering cross-section is $\simeq 1\,\mathrm{cm^2\,g^{-1}}$, at the scale of dwarf galaxies SIDM models can solve both the too-big-to-fail and the core-cusp problems (Zavala et al. 2013). Moreover, it has been shown that SIDM can explain the diverse shapes of galaxy rotation curves (Kamada et al. 2017) and at the same time be consistent with observations of galaxy clusters.

However, it is important to point out that the majority of previous works uses dark-matter-only simulations and thus ignore the interplay of self-interactions and baryonic physics. Kaplinghat et al. (2014) found through analytic calculations that for baryon-dominated systems, the thermalization can significantly increase the SIDM central density, with the inner halo shape following the baryonic potential. Recently, Elbert et al. (2018) and Sameie et al. (2018) used isolated simulation with an analytic galactic or disc potential in order to characterize the combined effect of SIDM and the main galaxy on the density profiles. They found that the cross-talk between dark matter and baryons leads to a variety of halo profiles, depending on the strength of the self-interaction and the galaxy properties; in particular, the presence of a compact stellar disc can lead to an increase of the overall central density through the core-collapse of the SIDM halo even beyond the CDM density (Koda & Shapiro 2011).

The aim of this work is to go one step further, by studying the baryonic effects not in an isolated and idealized scenario, but in full cosmological simulations to complement the efforts done in this regard in the past (Di Cintio et al. 2017; Robles et al. 2017; Harvey et al. 2018; Lovell et al. 2018). Some recent works in this direction (Robertson et al. 2018a, b) concentrated on galaxy clusters, while here we focus on the mass range that goes from Milky-Way-like to massive elliptical galaxies. For this purpose we use high-resolution re-simulations of lens analogues from the Illustris simulation (Vogelsberger et al. 2014a, c), carried out in CDM and SIDM and with a realistic model for baryonic physics. We adopt a viable SIDM scenario with a constant cross-section of $\sigma_T/m_\chi = 1\,\mathrm{cm^2\,g^{-1}}$ (model SIDM1 from Vogelsberger et al. 2014b). We study the properties of simulated SIDM haloes, compare them with their CDM counterparts and then focus on the differences in the lensing signal from the two models.

The paper is organized as follows: we describe the simulations in Section 2 and in Section 3 we analyse the properties of the haloes as a whole and of the central galaxy. In more detail, Section 3.1 focuses on the properties of the sample at the final snapshot of our simulations ($z = 0.2$), while in Section 3.2 we discuss how these are related with the halo evolution history; Section 3.3 explores the impact of SIDM on lensing observables. In Section 4 we study the subhalo population. Finally, we draw our conclusions in Section 5.

2 SIMULATIONS

This section describes how we have created a sample of nine simulated galaxies. The selection was performed by Despali & Vegetti (2017) on galaxies from the large-scale cosmological simulation Illustris (Genel et al. 2014; Torrey et al. 2014; Vogelsberger et al. 2014a), which was carried out using the AREPO hydrodynamical code (Springel 2010). Illustris reproduces observed quantities, such as the observed galaxy stellar mass function (Torrey et al. 2014), the stellar mass–halo mass relation (Genel et al. 2014), and the star

formation rate–stellar mass relation (Genel et al. 2014; Sparre et al. 2015).

Despali & Vegetti (2017) selected early-type galaxies (ETGs) at $z \simeq 0.2$ to resemble strong gravitational lenses from the SLACS survey (Bolton et al. 2006), in terms of total mass, stellar mass, stellar effective radius, and velocity dispersion. From this original selection, we identified a subsample of nine galaxies to re-simulate for this work.

The SLACS survey was optimized to spectroscopically identify strong gravitational lens systems with bright ETGs as deflectors. It has found nearly 100 lenses and lens candidates, among which a subsample of 53 lenses have confirmed ETG morphology: these have well-determined central stellar velocity dispersion, stellar masses ranging from $10^{10.5}$ to $10^{11.8}\,\mathrm{M_\odot}$ (Auger et al. 2009) and estimated total masses of the order of $10^{13}\,\mathrm{M_\odot}$ (Auger et al. 2010a), as well as central projected masses determined from strong lensing.

We have then re-simulated the subsample of nine galaxies with the zoom simulation method described in Sparre & Springel (2016). In our zoom simulations the dark matter mass resolution is $4.4 \times 10^6\,\mathrm{M_\odot}$, while the baryonic resolution is $9.1 \times 10^5\,\mathrm{M_\odot}$. We use the IllustrisTNG physics model, which has a novel treatment of low-accretion rate black hole feedback (Weinberger et al. 2017) and retuned galactic wind parameters (Pillepich et al. 2018) in comparison to the original Illustris model (which is presented in Vogelsberger et al. 2013). The IllustrisTNG model was used in our re-simulations because it produces more realistic gas fractions and gas properties of massive galaxies and galaxy clusters than the original Illustris simulation model (Pillepich et al. 2018; Vogelsberger et al. 2018b). As a consequence, some of the systems have a different morphology with respect to the original Illustris run, as it is detailed later on in the text. We use this increased variety in our sample generated by the new baryonic physics model: we investigate the effect of different galaxy morphologies on the dark matter distribution in the SIDM and CDM scenarios. Finally, we analyse the lensing properties of both early- and late-types in our sample.

The AREPO code has been extended to include both elastic and multistate inelastic SIDM (Vogelsberger et al. 2012, 2016, 2018a). Here we employ the elastic SIDM scheme with a constant cross-section. Specifically, each of our selected galaxies has been re-simulated both in a CDM and SIDM scenario with a constant cross-section of $\sigma_T/m_\chi = 1\,\mathrm{cm^2\,g^{-1}}$. The properties of the simulated haloes are summarized in Table 1.

3 PROPERTIES OF THE MAIN GALAXY

In this section, we first analyse our sample at redshift $z = 0.2$ (Section 3.1) and then explore the connection between the final halo properties and the halo evolution history (Section 3.2). Finally, we show the impact of SIDM on the distribution of the lensing observables (Section 3.3).

3.1 Mass distribution at $z = 0.2$

Table 1 summarizes the main properties of the nine simulated haloes at redshift $z = 0.2$. The systems are ranked by total halo mass M_{vir} (i.e. the mass within the radius that encloses a virial overdensity at the redshift considered, defined following Bryan & Norman 1998). In general, the total halo mass differs only by a few per cents between the two runs and the total stellar mass of the central galaxies is also very similar. The disc mass and thus the disc to total mass ratios (D/T) were calculated using the stellar circularities, as in previous

Table 1. Summary of halo properties: total halo mass $M_{\rm vir}$, virial radius $r_{\rm vir}$, stellar mass of the central galaxy M_*, stellar effective radius, and disc/total mass ratio (D/T). The last column shows the colour used to represent each halo throughout the paper (in the plots where different systems are shown together); the colours are the same for corresponding haloes in the CDM and SIDM runs. The systems are ranked by total halo mass ($M_{\rm vir}$); the last three systems have a developed disc in the CDM run (compact for systems 7 and 8, more extended and massive for system 9), while the others are classified as ETG-analogues.

		CDM run					
ID	ID(original)	$M_{\rm vir}[M_\odot]$	$r_{\rm vir}$ [kpc]	M_*(gal)$[M_\odot]$	$r_{\rm eff,*}$ [kpc]	D/T ($z = 0.2$)	colour
1	51	$3.73\ 10^{13}$	936	$4.08\ 10^{11}$	18.71	0.065	■
2	70	$2.45\ 10^{13}$	815	$2.71\ 10^{11}$	11.21	0.151	■
3	120	$1.64\ 10^{13}$	713	$2.16\ 10^{11}$	13.45	0.061	■
4	140	$1.4\ 10^{13}$	678	$3.03\ 10^{11}$	17.19	0.095	■
5	113	$9.07\ 10^{12}$	584	$1.46\ 10^{11}$	5.07	0.053	■
6	269	$7.61\ 10^{12}$	551	$2.06\ 10^{11}$	10.33	0.085	■
7	496	$4.60\ 10^{12}$	466	$9.33\ 10^{10}$	6.97	0.278	■
8	486	$4.26\ 10^{12}$	455	$1.06\ 10^{11}$	6.86	0.240	■
9	388	$3.00\ 10^{12}$	403	$1.74\ 10^{11}$	13.32	0.409	■

|		SIDM run					
ID	ID(original)	$M_{\rm vir}[M_\odot]$	$r_{\rm vir}$ [kpc]	M_*(gal)$[M_\odot]$	$r_{\rm eff,*}$ [kpc]	D/T ($z = 0.2$)	color
1	51	$3.76\ 10^{13}$	939	$4.50\ 10^{11}$	19.26	0.084	■
2	70	$2.46\ 10^{13}$	813	$3.02\ 10^{11}$	13.5	0.192	■
3	120	$1.65\ 10^{13}$	713	$1.75\ 10^{11}$	18.78	0.054	■
4	140	$1.41\ 10^{13}$	676	$3.04\ 10^{11}$	18.38	0.107	■
5	113	$8.64\ 10^{12}$	574	$1.42\ 10^{11}$	5.64	0.116	■
6	269	$7.51\ 10^{12}$	548	$2.14\ 10^{11}$	14.40	0.096	■
7	496	$4.42\ 10^{12}$	459	$7.81\ 10^{10}$	7.02	0.284	■
8	486	$3.95\ 10^{12}$	441	$9.31\ 10^{10}$	5.10	0.099	■
9	388	$2.98\ 10^{12}$	403	$1.85\ 10^{11}$	11.66	0.342	■

works (Scannapieco et al. 2009; Marinacci, Pakmor & Springel 2014; Snyder et al. 2015; Teklu et al. 2015; Grand et al. 2017) and in the same way that led to the selection from Despali & Vegetti (2017). In more details, the classification is based on the specific angular momentum through the parameter $\varepsilon = J_z/J(E)$, where J_z is the specific angular momentum and $J(E)$ is the maximum local angular momentum of the stellar particles: the fraction of stars with $\varepsilon > 0.7$ is a common definition of the disc mass and we adopt it for this work. Halo 9 was explicitly selected to host an extended and massive disc, and thus it is by construction not an analogue of the SLACS lenses. On the other hand, Halo 7 and Halo 8 had a disc mass component below 20 per cent in the original Illustris run, but they develop a more massive disc in the new CDM run with the IllustrisTNG model and so we classify them as disc-galaxies in this work. In the SIDM run, the disc component of system 8 at the final time is much smaller, while the other two systems maintain a similar morphology as in the corresponding CDM run. From this point of view, Systems 1 to 6 can instead be classified as ETGs in both runs.

The left-hand panel of Fig. 1 shows the position of our systems in the $r_{\rm eff}^* - M_*$ plane. Each system corresponds to a different colour – this colour scheme is maintained throughout the whole paper when the haloes are shown together (see Table 1). In general, the IllustrisTNG model produces lower stellar masses (at fixed halo mass – Pillepich et al. 2018) and smaller sizes (at fixed stellar mass – Genel et al. 2018): this explains why the systems from the CDM run (coloured triangles) tend to lie below the mean relation for the SLACS lenses, while the corresponding systems in the original Illustris simulations were more uniformly distributed around it. However, all the galaxies (except for system 9, by construction) still fall within the scatter from the SLACS mean relation in the CDM

run. We note that the most massive systems become more extended in the SIDM run, i.e. they have larger effective radii, while their stellar mass only changes by a few per cent. The right-hand panel of Fig. 1 shows the same points as the left-hand panel, but colour-coded according to the properties of the SIDM density profile, as we will detail in the following paragraph.

We now look at the dark matter and total matter distribution in the SIDM and CDM runs. The top panels of Fig. 2 shows the dark matter radial density profiles of the haloes in both runs: the CDM density is shown by the solid lines of different colours, while the dashed lines stand for the SIDM run. The small middle (lower) panels show the ratio of the SIDM to CDM dark matter (total mass) density profiles. We measure the mean central density within 15 kpc in both runs (also see Figs 5 and 7) and we use it as a proxy to divide the haloes in two categories: the systems in which the SIDM mean central density is lower than the CDM one are shown in the left-hand panels (hereafter 'CORED' systems), while those in which the central density is higher in SIDM are shown in right-hand panels (hereafter 'CUSPY' systems). Thus, the haloes are in practice classified according to the properties of the SIDM density profile. It is interesting to note that the difference between the SIDM and CDM density profiles is stronger for the CUSPY systems than for the CORED ones, especially when looking at the dark matter density profile (middle panels).

The same classification applies to the right-hand panel of Fig. 1, where the points in the $r_{\rm eff}^* - M_*$ plane are colour-coded according to whether they belong to the CORED or CUSPY categories. In general, the green and red squares in the right-hand panel occupy two different parts of the parameter space. The four CUSPY systems occupy the lower left part of the $r_{\rm eff}^* - M_*$ plane: they have lower stellar masses and, most importantly, their stellar distributions are
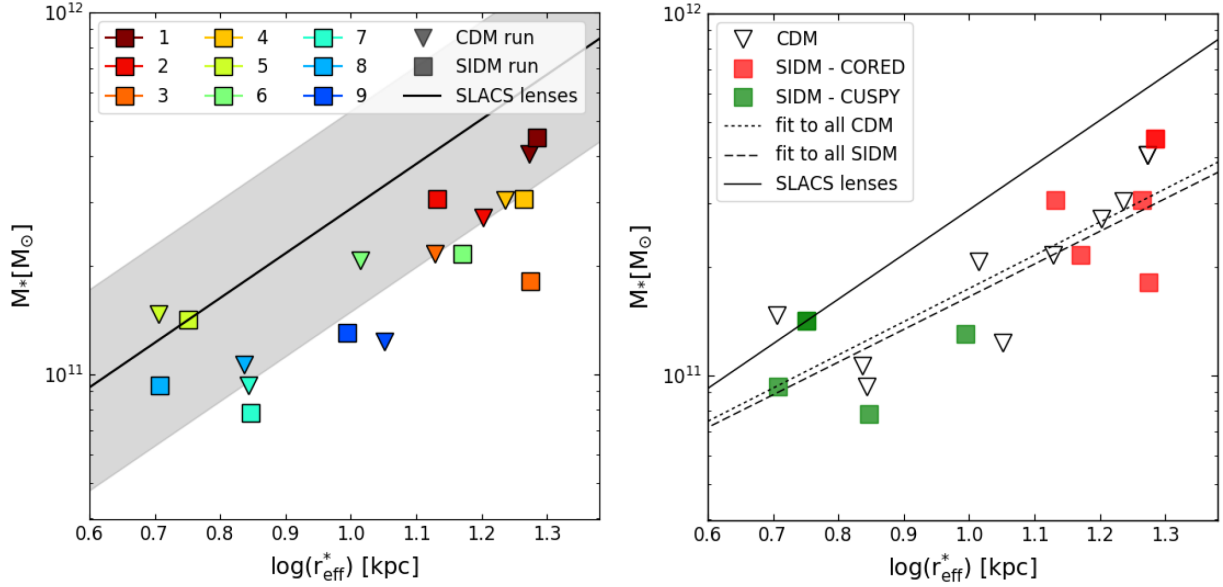
Figure 1. Halo sample in the r_{eff}^*-M_* plane at $z = 0.2$. The black solid line shows the mean relation derived for the SLACS lenses by Auger et al. (2010b), together with the scatter of the data (grey band) calculated from the intrinsic scatter of the data and the uncertainty on the linear fit. Left-hand panel: the coloured squares and triangles show how the halo properties change between the CDM and SIDM run. Right-hand panel: we show the same points as in the left-hand panel, but here the systems are colour-coded according to the final profile properties; the dotted and dashed black lines show the best-fitting linear relation to the full sample of CDM and SIDM haloes, respectively.
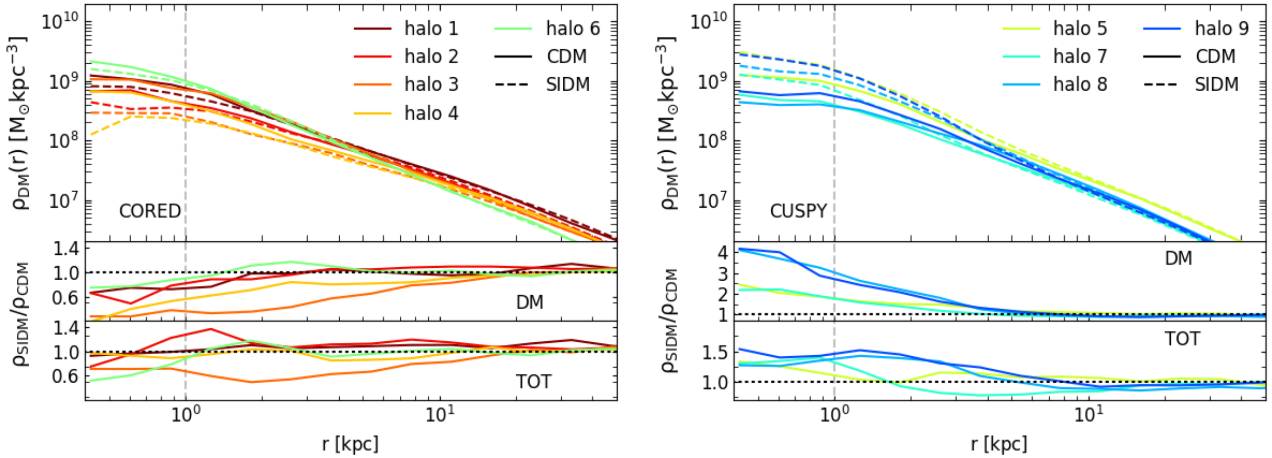
Figure 2. Radial density profiles of the main galaxy at $z = 0.2$. The CORED systems are shown in the left-hand panels, while the CUSPY ones in the right-hand panels. In the top panels, solid (dashed) lines show the dark matter profile for the CDM (SIDM) run. The ratio between the dark matter and total profiles in the two runs is shown in the middle and bottom residuals panel. We focus on the inner region of the haloes where the SIDM effects are stronger; the profiles are identical in the outer parts ($r > 0.1 \times r_{vir}$). The grey vertical like marks the spatial resolution of the simulations, within which interpretation requires care.

more compact. A cuspy profile is found in the disc galaxies, but also in the most compact of the ETGs-like systems (halo 5). In this respect, it is of particular interest to compare systems 5 and 6 which, despite having almost identical total and stellar masses in both scenarios, evolve differently in the SIDM run: the stellar effective radius of system 5 is about half of that of system 6, supporting the fact that a very compact baryonic component can dominate the total density profile and drive the growth of a cuspier dark matter density. This suggests that, apart from the morphological type and the presence of a disc (as in Sameie et al. 2018), a significant role

could be played by the halo and galaxy mass and thus its mass accretion history. We investigate this hypothesis in the next section.

We now fit the dark matter density radial distribution with the Einasto profile (Einasto 1965), defined as

$$\rho(r) = \rho_{-2} \exp\left\{-2\alpha\left[\left(\frac{r}{r_{-2}}\right)^{1/\alpha} - 1\right]\right\}, \tag{1}$$

where ρ_{-2} and r_{-2} are the density and the radius at which $\rho(r) \propto r^{-2}$ and α defines the steepness of the power law. The Einasto profile
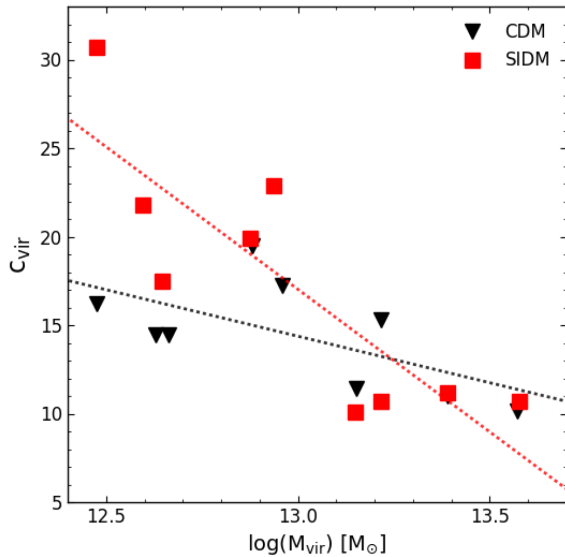
Figure 3. Concentration–mass relation at $z = 0.2$: c_{vir} is calculated from the best-fitting Einasto profile. The black and red dotted lines show the best-fitting linear relation for the CDM and SIDM runs, respectively.

provides a good fit to both the CDM and SIDM haloes, since it is able to well describe different inner slopes. For the CDM haloes, both the NFW and the Einasto profiles provide a good fit, while the NFW profile is not a good fit for cored SIDM haloes; in general, self-interaction produces a larger variety of profile shapes and thus a more flexible definition for the profile is needed. Thus, in what follows we use the Einasto profile for both runs.

Fig. 3 shows the concentration–mass relation in the two runs: the CDM haloes are represented by the black triangles, while the SIDM ones by the red squares. The dotted lines of corresponding colour show the best-fitting linear relation between $c_{vir} = r_{vir}/r_{-2}$ and $\log(M_{vir})$. The concentrations of our sample are higher than the average concentration–mass relation at $z = 0.2$ (Macciò et al. 2007; Duffy et al. 2008), due to a combination of two effects: (i) the dark matter concentrations in hydrodynamical simulations are altered by the presence of baryons and in particular the IllustrisTNG models produces higher concentrations than in the dark-matter-only run (due to adiabatic contraction of the halo as it responds to the assembly of the galaxy) in the halo mass range spanned by our sample (Lovell et al. 2018) – this effect is enhanced in our case for the CUSPY systems; (ii) we selected analogues of strong lenses, which are in general more concentrated than average at fixed mass (Giocoli et al. 2013). While for CDM the concentration–mass relation is, as usual, a slowly declining function of mass, the SIDM relation is much steeper and thus the haloes show a greater diversity of profiles, in the sense that the SIDM concentrations span a wider range of values than the CDM ones over our limited mass range. This is qualitatively similar to what was found by Robertson et al. (2018b) by looking at SIDM + baryons simulations of cluster-mass haloes. Again, we note how halo 6 follows the behaviour of CORED haloes, while halo 5 that of CUSPY haloes, even though their masses and disc fractions are almost identical in both runs (see Table 1). This suggests that, together with the morphological type and halo mass, something else contributes to shape the final properties of the profile. We investigate this in the next section.

3.2 Link to the halo evolution

Fig. 4 shows the mass accretion history of all the systems from redshift $z = 3$ to the final snapshot of the simulation at $z = 0.2$, calculated by following the main progenitor back in time. Results from the CDM and SIDM runs are shown, respectively, by the solid and dashed lines; the haloes are again divided in CORED (left-hand panel) and CUSPY (right-hand panel) systems, as in Fig. 2. Qualitatively, the two groups of systems behave differently: the CORED systems experience a fast accretion phase at low redshift (late assembly), while the CUSPY systems have a more regular history (early assembly). The accretion history in CDM and SIDM is shown, respectively, by solid and dashed lines: interestingly, in most cases the history of each halo is almost identical in CDM and SIDM, indicating that the mass accretion proceeds similarly (both for DM and baryonic components) since it is regulated by the matter distribution on larger scales, but in the two scenarios it has a different effect on the inner structural properties of haloes. If we define the halo formation time z_f as the redshift at which the halo mass was already half of the final one in the main progenitor branch (Lacey & Cole 1994; Giocoli et al. 2013), we find that our two categories are also separated in z_f. The formation redshift z_f of each halo is the same in both runs, due to the similarity in the mass accretion history. The value of z_f correlates with the differences in the dm-profile between the two runs: Fig. 5 shows z_f as a function of the mean ratio of the central density, measured within 15 kpc from the centre. The coloured points show the position of each system and the solid grey line is the best-fitting linear relation between the two quantities, which represents well the general trend. The two dotted lines separate the regions of the parameter space into (i) CORED versus CUSPY (vertical) and (ii) $z_f < 1$ versus $z_f > 1$ (horizontal).

Fig. 6 shows the evolution with redshift of the mean central density in dark matter of all the sample in the CDM (left-hand panels) and SIDM (right-hand panels) scenarios. The y-axis shows the mean value of $\rho_{DM}(z)/\rho_{DM}(z = z_f)$, measured in the inner 15 kpc from the centre ($1 < r < 15$ kpc) as in Fig. 5. The formation redshift z_f is marked by a coloured circle for each halo. While for CDM the central density steadily increases with time, in SIDM this is true only for the CUSPY haloes; the central density in most of the CORED systems oscillates around $\rho_{DM}(z = z_f)$ with an irregular and more complex behaviour, in particular at $z < z_f$.

Our sample is not large enough to fully characterize the halo evolution, but we believe that it spans a range in mass and morphology that is wide enough to derive a consistent picture. The correlation between the mass accretion history and the properties of the final density profile suggests that in the CUSPY systems the baryons drive the evolution of the central dark matter core – created at an earlier time by the DM self-interaction (since haloes are assembled earlier) – and the interplay between baryons and dark matter leads to the final cuspy profile. The more massive haloes, belonging to the CORED category, formed at redshift $z \leq 1$ and thus we see them at the stage in which the large central core is just established. Moreover, a very compact stellar component (and the morphology of the central galaxy, i.e. the presence of a stellar disc) enhances the different behaviours, contributing to the formation of an even cuspier profile, while this is not the case for the more extended baryonic distribution of the ETGs (see the effective radii in Fig. 1). In order to better visualize these behaviours, in Fig. 7 we show the dark matter density profile of three haloes from our sample, from $z = 3$ to $z = 0.2$. The top row shows the evolution in the CDM run, which is qualitatively similar for all the haloes in our sample: the main progenitor dark matter central density increases with time:
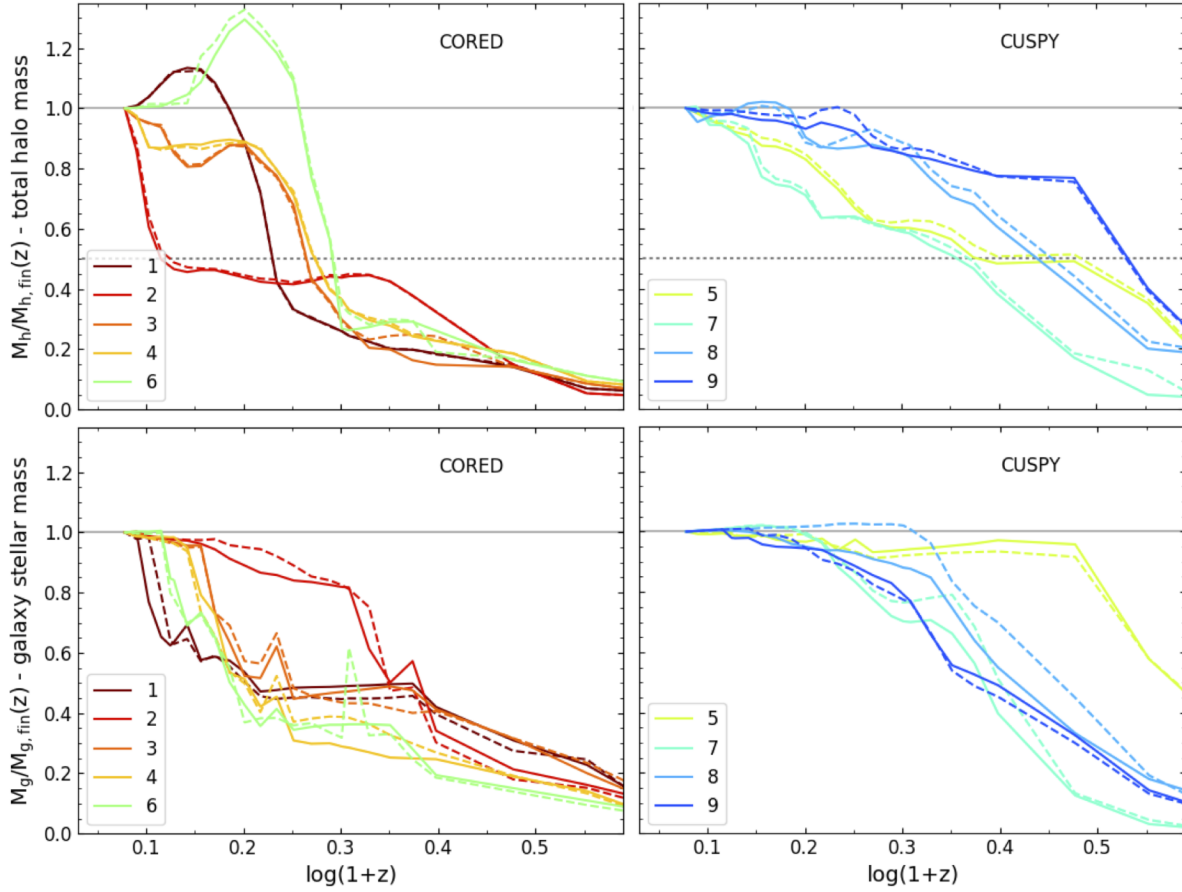
Figure 4. Mass accretion history. Results from the CDM and SIDM runs are shown, respectively, by the solid and dashed lines; the haloes are again divided in CORED (left-hand panel) and CUSPY (right-hand panel) systems, as in Fig. 2. We show the accretion history of both the halo (total mass within $R_{\rm vir}$) and of the stellar mass of the main galaxy. In the top panels, the formation redshift of the haloes (z_f) correspond to the moment at which the coloured lines intersect the horizontal grey dotted thresholds, corresponding to half of the final halo mass.
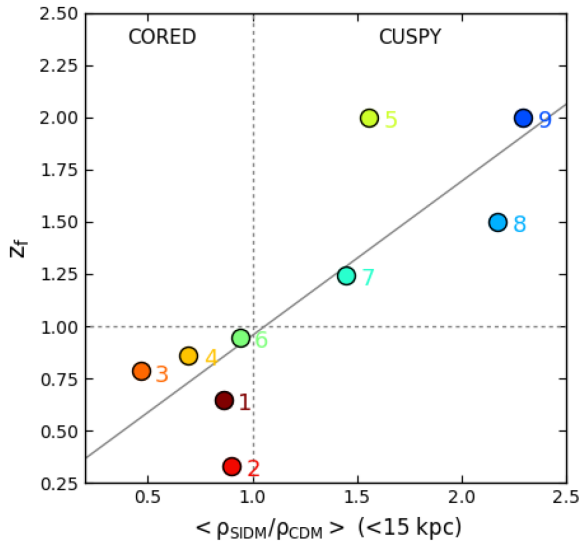

Figure 5. Correlation between the properties of the density profile and the halo formation time. The *x*-axis shows the mean ratio of the dark matter density at $1 < r < 15$ kpc between the two models, while z_f is defined as the redshift at which the halo had accreted 50 per cent of its final mass.

The second row shows the corresponding profiles in the SIDM run. In this case, there is a larger halo-to-halo variation. The SIDM dark matter density profile of Halo 2 (CORED) clearly oscillates with time, going through an initial growth phase ($z > 2$) during which the stellar distribution becomes more compact and the central density increases, followed by the creation of a central core ($0.8 \leq z \leq 2$) and by a final phase in which the central density rises again. In the other CORED systems, the oscillations of the central density are less pronounced, but consistent with the same behaviour. On the other hand, Halo 9 shows one of the cuspiest SIDM profiles in our sample and in this case, the SIDM dark matter profile grows monotonically as in CDM and reaches a higher central density, suggesting that the presence of a disc galaxy triggers an evolution similar to the one seen in Sameie et al. (2018). Nevertheless, in the same work it is also claimed that compact stellar discs have a stronger effect than extended ones. Our simulations seem to suggest once again that, in the presence of a realistic baryonic physics model, the co-evolution of the two components is more complex: as can be seen from Table 1, the central galaxy of Halo 9 has a more massive and extended disc with respect to systems 7 and 8, but the total variation of the density profile is similar. Finally, Halo 5 (middle column) belongs to the CUSPY category at $z = 0.2$, but has an intermediate total and stellar mass. In this case, the evolution of the density profile is also somehow in between the two categories
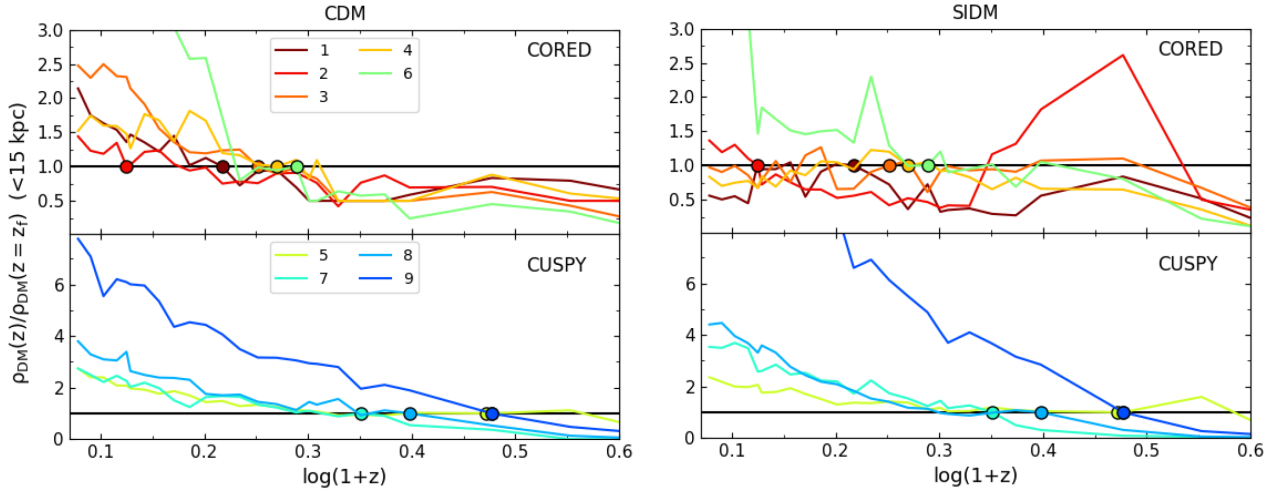
Figure 6. Evolution with redshift of the mean central density in dark matter in the CDM (left) and SIDM (right) scenarios. Each coloured line stands for one of the haloes in the sample and the points of corresponding colour mark $z = z_f$. While for CDM the central density steadily increases with time, in SIDM this is true only for the CUSPY haloes.
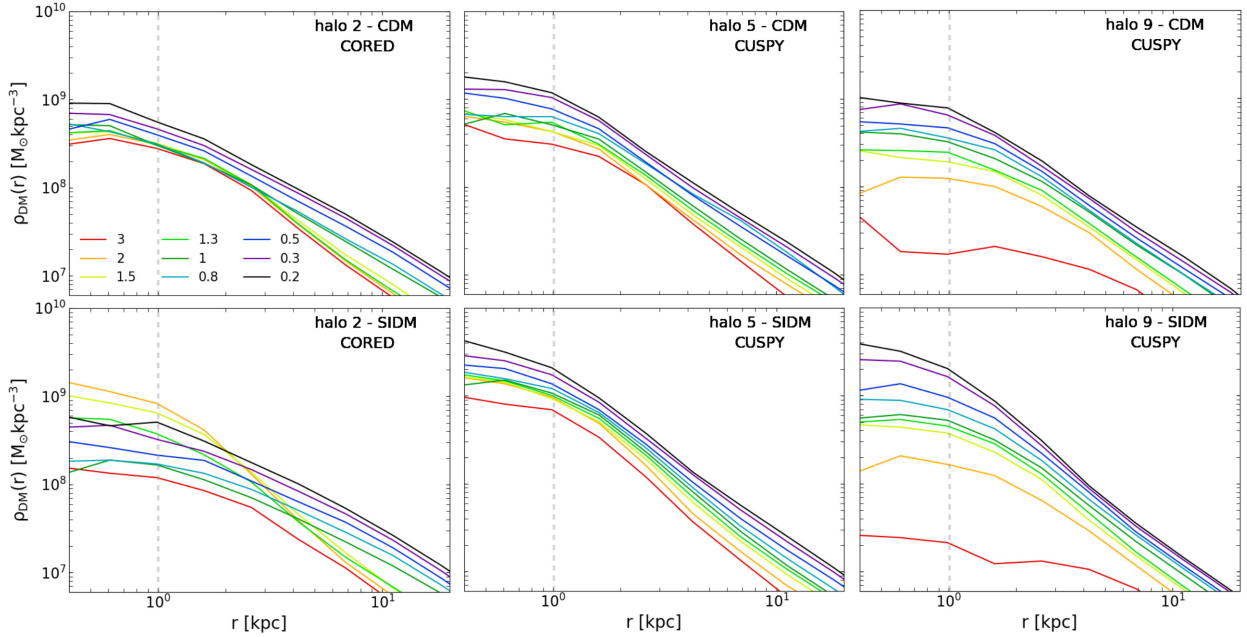
Figure 7. Evolution with redshift of the inner part of the density profile ($1 < r < 15$ kpc) with redshift in the CDM (first row) and SIDM (second row) runs. We show three haloes, as an example of the three main behaviours. The grey vertical like marks the spatial resolution of the simulations, within which interpretation requires care.

since the final SIDM profile has a slightly cuspier final profile and a higher central density, but not as extreme as Halo 9.

3.3 Lensing properties

Since gravitational lensing allows to measure the total projected mass distribution of the deflectors directly, the results presented in the previous sections may have direct consequences on the distribution of the main lensing observables, such as the Einstein radii r_E.

We use the lensing code GLAMER (Metcalf & Petkova 2014; Petkova, Metcalf & Giocoli 2014) to create realistic mock images from the simulations. Using the particle positions and masses,

GLAMER calculates the projected surface mass density and thus the convergence, magnification, and deflection angles created by the main lens with a tree algorithm. Each particle is represented with a B-spline in three dimensions as is commonly done in smooth particle hydrodynamics (SPH) simulations. The dark matter particles in simulations are point-like, but in order to avoid unrealistic deflections of the light rays, their mass has to be 'smoothed', i.e. distributed on a larger physical scale, according to their surrounding density so that the halo appears as a continuous mass distribution. The size of the smoothing length is set to the distance to the N_{smooth}-th nearest neighbour where N_{smooth} can be adjusted – in this work $N_{smooth} = 64$. This scheme provides smaller smoothing lengths where the particles are dense (for example at the centres of haloes) and it is justified
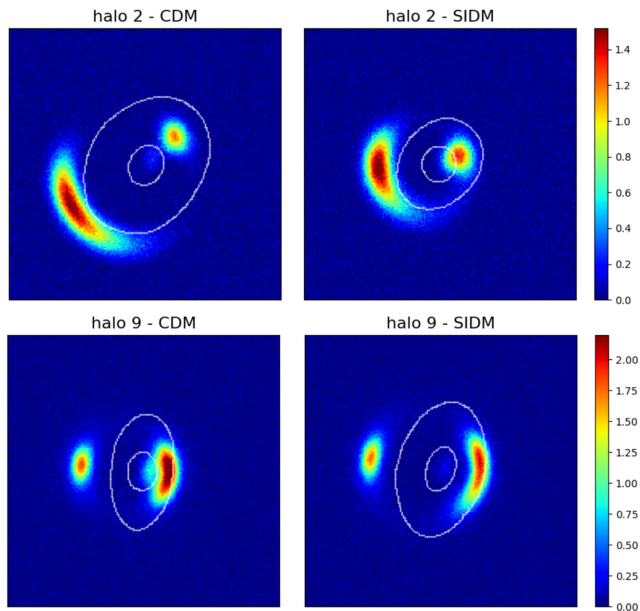
Figure 8. Mock lensed images created from two of the simulated haloes, for a simulated source at $z = 1$. The source is a mock image of an ETG from the Illustris simulation, created in the ACS-F606 filter, using the technique described in Torrey et al. (2015); we used the same source, located in the same position with respect to the centre of the image plane, for the four cases. It has then been convolved with an *HST*-like point spread function and a realistic Gaussian noise has been added. The critical lines are shown in white; all the images are 5 arcsec on a side.

by a large number of particles, and larger ones where the particles are sparse and shot noise would otherwise be a problem. A similar approach is followed also for the baryonic cells, since GLAMER is not able to take into account the shape of each individual cell.

We ran the ray-tracing code through 200 different random projections for each halo to have a good statistical sample; the lens and source redshifts are set, respectively, to $z_L = 0.2$ and $z_S = 1$. Fig. 8 shows examples of the mock images created with a simulated background source, for two haloes in the sample; the images are 5 arcsec wide and the critical lines (in white) are superposed to the surface brightness distribution of the lensed images.

From each of the mock images, we estimated the Einstein radius r_E, whose size provides a way to quantify the magnitude of the lensing power of the halo. In the top panels of Fig. 9, we show the distribution of the Einstein radii for the CDM (left) and SIDM (right) runs from the whole sample of mock images (i.e. 200 projections for each of the nine haloes). Then, we separate the haloes in two categories according to the properties of their SIDM density profile (middle) or the morphological classification of the main galaxy (bottom), using the D/T fractions reported in Table 1. In the CDM run, the last three haloes are classified as discs, while in SIDM halo 8 has a much smaller disc component and thus belong to the other category. The median Einstein radii of the two distributions are shown by the dashed (for CUSPY or discs) and solid (for CORED or ETGs) vertical lines. The Einstein radii of ETGs peak at lower values in SIDM than in CDM, due to their cored density profiles. In particular, due to the central density cores in ETGs, the SIDM distribution lacks the largest Einstein radii. It is also interesting to note that in SIDM the median Einstein radius of CORED and CUSPY systems are in practice identical and that the two distributions superpose: the bi-modality seen in CDM is in

general lost in the SIDM run. These results seem to suggest that the observed distribution of Einstein radii in a large survey such as EUCLID could in principle allow us to distinguish between SIDM and CDM and provide an independent probe of the nature of dark matter. In practice, a wider distribution of source and lens redshifts and a wider sample of simulated galaxies resembling that predicted for EUCLID or other wide-field surveys should be used to test whether our current results hold in a realistic scenario.

In this respect, it is also interesting to note that some properties of systems 3 and 6 do not match the ones of SLACS lenses: even if they can be classified as early-types, their sizes are larger than the SLACS ones and they lie farther away from the mean relation shown in Fig. 1, which in turn corresponds to the fact that their Einstein radii are smaller in SIDM than in CDM. Thus, had the selection been done directly on the SIDM run, they might not have been chosen as SLACS analogues.

4 SUBHALO POPULATION

In this section, we study the properties of the subhaloes in our sample. In particular, we measure the subhalo mass function in the two runs and we compute the subhalo density profiles. SIDM models are often mentioned alongside WDM as able to resolve a number of discrepancies between observations and numerical simulations. Moreover, the presence of the self-interaction can alter the number density and the properties of subhaloes, and with them their detectability through gravitational lensing (Vegetti et al. 2010, 2012, 2014; Hezaveh et al. 2016; Birrer et al. 2017; Li et al. 2017; Despali et al. 2018)

In the top panel of Fig. 10 we show the subhalo mass function for all the subhaloes with a mass $M_{sub} > 10^8 \, M_\odot$, while in the bottom panel we plot the ratio of the number counts in the two runs for each halo and the mean and median ratios (solid and dashed black lines). For the SIDM model used in this work, we find no significant difference in the subhalo counts with respect to the CDM scenario. This result is in agreement with previous findings from Zavala et al. (2013) and Rocha et al. (2013). In particular, Zavala et al. (2013) have found that a much higher cross-section ($10 \, cm^2 \, g^{-1}$) is necessary to have a significant suppression in the number of subhaloes; at the same time, they found that a much lower cross-section of $0.1 \, cm^2 \, g^{-1}$ is in this context indistinguishable from CDM. Recently, Díaz Rivero et al. (2018) have measured the subhalo power spectrum in CDM and the ETHOS model (Vogelsberger et al. 2016) from maps of projected mass density (convergence), finding a clear suppression and thus suggesting that gravitational lensing might be used to distinguish the two scenarios. However, it should be pointed out that this result is not related to the presence of self-interaction (too weak to suppress the number density in their model), but mainly to a truncation of the initial power spectrum at the small scales. Thus, while in general velocity-independent SIDM models with a low cross-section do not affect the number of subhaloes in an appreciable way, it may be that more complicated models that include other effects other than self-interaction – such as velocity-independent cross-sections, inelastic scattering or dark radiation (Vogelsberger et al. 2016, 2018b) – may result in significant changes. Moreover, models including a truncated power spectrum may resemble WDM from the point of view of subhalo abundances.

In order to directly compare subhalo properties between the two runs, we selected the matching subhaloes using the particles IDs: if the matched subhaloes share more than 50 per cent of the mass, we consider the matching to be reliable. The masses of the
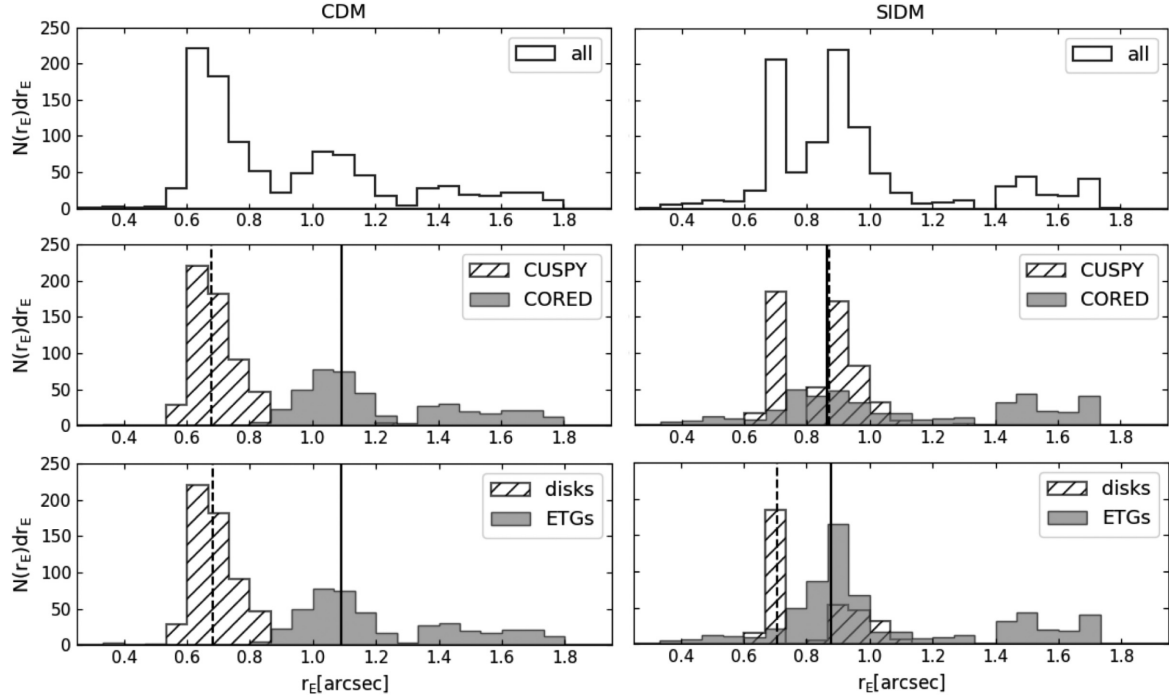
Figure 9. Einstein radii distribution for the ray-tracing runs in the CDM (left) and SIM (right) scenarios. The top panels shows the overall distribution derived from 200 random projections for each halo, while in the second and third rows galaxies are divided according to the properties of the corresponding SIDM density profile or their morphological type in each run (based on the D/T ratio). The vertical solid and dashed lines show the medians for the two populations.
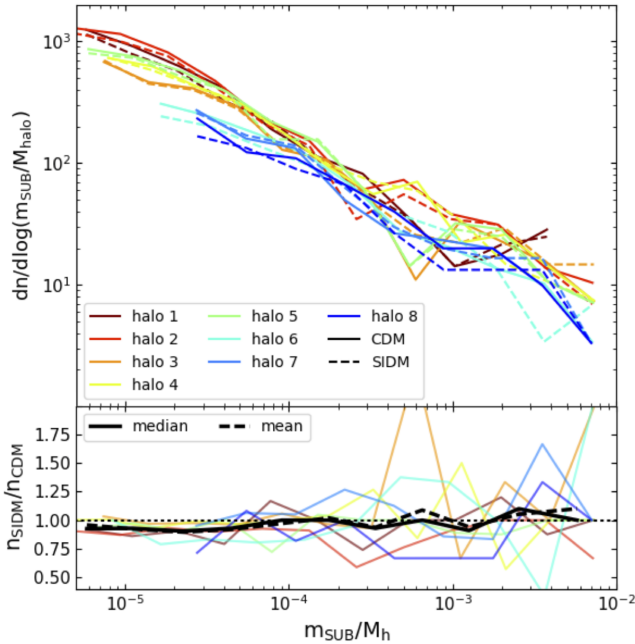
Figure 10. Subhalo mass function. In the top panel we show the subhalo mass function of the simulated haloes, both in the CDM (solid lines) and SIDM scenarios (dashed lines). The ratio between the number counts in the two runs is shown in the bottom panel: on average, there is no significant difference in the subhalo number counts, as can be seen from the mean ratio (solid black line).

matched systems are on average the same in the two runs, with a maximum difference of about 15–20 per cent. We measured the total density profiles of each pair and then checked whether the slope of the profile is different: Fig. 11 shows the median ratio
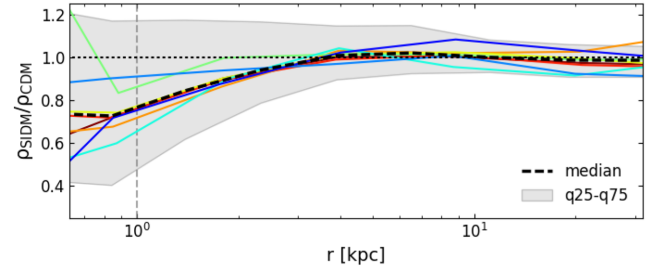
Figure 11. Ratio of the subhalo density profiles, for systems with N_{part} > 500. The median ratio for each halo is shown by a different colour, while the median ratio for the whole sample is represented by the black dashed line. The grey shaded area encloses the region between the 0.25 and 0.75 quantiles. The grey vertical line marks the spatial resolution of the simulation, within which interpretation requires care.

of the subhalo density profiles of matched subhaloes. We use only the subhaloes with more than 500 particles, corresponding to $M_{sub} \geq 1.4 \times 10^9 \, M_\odot$, in order to have a reliable estimate of the density profile. The median central density of subhaloes is at most 20 per cent lower in the SIDM scenario (black dashed line) for the region in which the profile can be trusted. However, the grey shaded region marks the region enclosed between the 0.25 and 0.75 quantiles, still consistent with no differences between the two profiles. Given that our sample is limited, we can only conclude that we expect little difference in the lensing signal caused by subhaloes and thus on their detectability through lensing, between this model and CDM. However, other SIDM models may cause stronger effects on the subhalo profiles (as on their abundances), creating a further degeneracy with WDM models. Detailed studies including different SIDM models are necessary to fully understand how well SIDM, WDM, and CDM can be discriminated on the basis

of the subhalo number density and of the corresponding lensing signal, in particular.

5 DISCUSSION

In this work, we have analysed a sample of simulated galaxies in CDM and SIDM scenarios, in order to understand the effects of dark matter self-interaction on the final halo properties. For this purpose, we selected nine galaxies from the Illustris (Vogelsberger et al. 2014a) simulation and re-simulated them in CDM and SIDM with the IllustrisTNG model for baryonic physics. Our sample consists of six ETGs (analogues of observed systems, such as the SLACS lenses) and three galaxies with a fairly important disc component (see Table 1). The main result of this work is that, in the presence of both dark matter self-interactions and baryonic physics, halo density profiles have a complex evolution and a larger variety of final properties than dark-matter-only SIDM simulations (or CDM simulations). Our analysis is generally consistent with the results from Sameie et al. (2018) and Robertson et al. (2018b), but using high-resolution hydrodynamical simulations allowed us to reach a deeper understanding of the halo evolutionary properties.

While in dark-matter-only SIDM simulations all haloes create a central core, with a size proportional to the strength of the self-interaction (Vogelsberger et al. 2014b), in the presence of baryonic physics only part of our sample shows a cored profile in the SIDM run (five out of nine simulated systems); four systems, on the contrary, have a cuspier profile in SIDM than in CDM (Fig. 1 and 2).

We divide the haloes in two categories (CORED and CUSPY), according to whether the final SIDM dark-matter density profile is flatter or steeper than the CDM one. We find that the final properties, such as the density profile, correlate with the merging history of the halo: CORED systems are in general more massive and formed at $z \leq 1$, showing a recent phase of fast accretion, while CUSPY systems formed at $z \geq 1$ (Fig. 4). The dark-matter density profiles also show a more complex evolution with time in the SIDM scenario: the central density oscillates in CORED systems, where the self-interaction acted recently to create a core, while the combination of early formation time and the presence of a disc increases the central density in CUSPY systems. A general consequence is that SIDM haloes possess a greater variety of density profiles and concentrations with respect to CDM.

The size of our sample is limited and thus we cannot draw statistically supported conclusions. Nevertheless, the systems span a range in halo properties (such as mass and morphological type) that is sufficient to retrieve a physically consistent picture. We confirm the conclusion from previous works (Kaplinghat et al. 2014; Sameie et al. 2018; Robertson et al. 2018b), that the baryonic physics has a stronger impact on the final density profile in SIDM models: this is demonstrated by the fact that the haloes can be efficiently classified in two separate categories based on their final properties. However, these final properties also correlate with the mass accretion history: systems with very similar mass and morphological types can belong to different categories and their behaviour can be understood in terms of the difference in the accretion history. This correlation suggests that in the CUSPY systems the self-interaction acted at earlier time, but then the baryons dominate the evolution of the density profile and the interplay between baryons and dark matter leads to the final cuspy profile. This effect is enhanced in the presence of a compact baryonic distribution (see the effective radii of CUSPY and CORED systems in Fig. 1) and the presence of a stellar disc, which drive an extra boost in the central dark matter density profile in SIDM simulations, with respect to systems with an ETG-like morphology. On the other hand, the more massive haloes (CORED) formed at redshift $z \leq 1$ and thus we see them at the stage in which the large central core is established. As a consequence of this complex interplay between SIDM and baryonic physics, also the lensing properties of our sample are different in the two runs. First of all, due to the presence of the central core, some of the most massive systems would not be classified as SLACS lens analogues (see Fig. 1) in SIDM. Moreover, the overall distribution of Einstein radii is different in the two scenarios. In CDM the overall distribution is clearly bi-modal and the contributions of ETGs-analogues and disc galaxies are separated, while in SIDM the mean Einstein radii of these two categories are closer to each other and the two distribution partially superpose. In particular, due to the central density cores in ETGs, the distribution lacks the largest Einstein radii. Our results suggest that future large surveys could provide a way to constrain the dark matter model and exclude some scenarios based on the overall distribution of lensing properties, even though a larger sample and a wider distribution of lens and source redshifts needs to be considered to confirm this result. We remark that different results might be obtained by using a reduced number of zoom simulations or a full cosmological simulation, as shown for instance in the discrepancies in the properties of SIDM haloes in the cluster mass range between the results of Robertson et al. (2018b) and Robertson et al. (2018a). Thus, our results should be extended to a full cosmological box in order to be confirmed.

Finally, we have analysed the subhalo population in the two runs. We find that the number density of subhaloes is not significantly different in the two considered scenarios: from a lensing point of view, this means that CDM and our adopted SIDM model could not be clearly distinguished with techniques such a gravitational imaging (Vegetti et al. 2010, 2014).

Our results clearly show that it is of fundamental importance to take into account the effects of baryonic physics, especially when comparing to observational results. In the future, the interplay between SIDM models and baryonic physics should be investigated using larger halo samples or cosmological simulations – and more SIDM models (for example with a velocity-dependent cross-section, ETHOS or inelastic models), in order to study its effect on a broader mass range.

REFERENCES

Astropy Collaboration, 2013, A&A, 558, A33

Auger M. W., Treu T., Bolton A. S., Gavazzi R., Koopmans L. V. E., Marshall P. J., Bundy K., Moustakas L. A., 2009, ApJ, 705, 1099

Auger M. W., Treu T., Gavazzi R., Bolton A. S., Koopmans L. V. E., Marshall P. J., 2010a, ApJ, 721, L163

Auger M. W., Treu T., Bolton A. S., Gavazzi R., Koopmans L. V. E., Marshall P. J., Moustakas L. A., Burles S., 2010b, ApJ, 724, 511

Birrer S., Welschen C., Amara A., Refregier A., 2017, J. Cosmol. Astropart. Phys., 4, 049

Bolton A. S., Burles S., Koopmans L. V. E., Treu T., Moustakas L. A., 2006, ApJ, 638, 703

Boylan-Kolchin M., Springel V., White S. D. M., Jenkins A., Lemson G., 2009, MNRAS, 398, 1150

Bryan G. L., Norman M. L., 1998, ApJ, 495, 80

Bullock J. S., Boylan-Kolchin M., 2017, ARA&A, 55, 343

Colín P., Avila-Reese V., Valenzuela O., Firmani C., 2002, ApJ, 581, 777

Davé R., Spergel D. N., Steinhardt P. J., Wandelt B. D., 2001, ApJ, 547, 574

Despali G., Vegetti S., 2017, MNRAS, 469, 1997

Despali G., Vegetti S., White S. D. M., Giocoli C., van den Bosch F. C., 2018, MNRAS, 475, 5424

Di Cintio A., Tremmel M., Governato F., Pontzen A., Zavala J., Bastidas Fry A., Brooks A., Vogelsberger M., 2017, MNRAS, 469, 2845

Díaz Rivero A., Dvorkin C., Cyr-Racine F.-Y., Zavala J., Vogelsberger M., 2018, Phys. Rev., 98, 103517

Duffy A. R., Schaye J., Kay S. T., Dalla Vecchia C., 2008, MNRAS, 390, L64

Einasto J., 1965, Trudy Astrofizicheskogo Instituta Alma-Ata, 5, 87

Elbert O. D., Bullock J. S., Kaplinghat M., Garrison-Kimmel S., Graus A. S., Rocha M., 2018, ApJ, 853, 109

Genel S. et al., 2014, MNRAS, 445, 175

Genel S. et al., 2018, MNRAS, 474, 3976

Giocoli C., Marulli F., Baldi M., Moscardini L., Metcalf R. B., 2013, MNRAS, 434, 2982

Grand R. J. J. et al., 2017, MNRAS, 467, 179

Harvey D., Revaz Y., Robertson A., Hausammann L., 2018, MNRAS, 481, L89

Hezaveh Y. D. et al., 2016, ApJ, 823, 37

Kamada A., Kaplinghat M., Pace A. B., Yu H.-B., 2017, Phys. Rev. Lett., 119, 111102

Kaplinghat M., Keeley R. E., Linden T., Yu H.-B., 2014, Phys. Rev. Lett., 113, 021302

Klypin A., Kravtsov A. V., Valenzuela O., Prada F., 1999, ApJ, 522, 82

Koda J., Shapiro P. R., 2011, MNRAS, 415, 1125

Lacey C., Cole S., 1994, MNRAS, 271, 676

Li R., Frenk C. S., Cole S., Wang Q., Gao L., 2017, MNRAS, 468, 1426

Lovell M. R. et al., 2012, MNRAS, 420, 2318

Lovell M. R. et al., 2017, MNRAS, 468, 4285

Lovell M. R. et al., 2018, MNRAS, 481, 1950

Lovell M. R., Frenk C. S., Eke V. R., Jenkins A., Gao L., Theuns T., 2014, MNRAS, 439, 300

Ludlow A. D., Bose S., Angulo R. E., Wang L., Hellwing W. A., Navarro J. F., Cole S., Frenk C. S., 2016, MNRAS, 460, 1214

Macciò A. V., Dutton A. A., van den Bosch F. C., Moore B., Potter D., Stadel J., 2007, MNRAS, 378, 55

Marinacci F., Pakmor R., Springel V., 2014, MNRAS, 437, 1750

Metcalf R. B., Petkova M., 2014, MNRAS, 445, 1942

Peter A. H. G., Rocha M., Bullock J. S., Kaplinghat M., 2013, MNRAS, 430, 105

Petkova M., Metcalf R. B., Giocoli C., 2014, MNRAS, 445, 1954

Pillepich A. et al., 2018, MNRAS, 473, 4077

Planck Collaboration, 2014, A&A, 571, A1

Robertson A. et al., 2018b, MNRAS, 476, L20

Robertson A., Harvey D., Massey R., Eke V., McCarthy I. G., Jauzac M., Li B., Schaye J., 2018a, preprint (arXiv:1810.05649)

Robles V. H. et al., 2017, MNRAS, 472, 2945

Rocha M., Peter A. H. G., Bullock J. S., Kaplinghat M., Garrison-Kimmel S., Oñorbe J., Moustakas L. A., 2013, MNRAS, 430, 81

Sameie O., Creasey P., Yu H.-B., Sales L. V., Vogelsberger M., Zavala J., 2018, MNRAS, 479, 359

Scannapieco C., White S. D. M., Springel V., Tissera P. B., 2009, MNRAS, 396, 696

Schneider P., 1992, A&A, 254, 14

Snyder G. F. et al., 2015, MNRAS, 454, 1886

Sparre M. et al., 2015, MNRAS, 447, 3548

Sparre M., Springel V., 2016, MNRAS, 462, 2418

Springel V., 2010, MNRAS, 401, 791

Teklu A. F., Remus R.-S., Dolag K., Beck A. M., Burkert A., Schmidt A. S., Schulze F., Steinborn L. K., 2015, ApJ, 812, 29

Astropy Collaboration, 2018, AJ, 156, 123

Torrey P. et al., 2015, MNRAS, 447, 2753

Torrey P., Vogelsberger M., Genel S., Sijacki D., Springel V., Hernquist L., 2014, MNRAS, 438, 1985

Vegetti S., Koopmans L. V. E., Bolton A., Treu T., Gavazzi R., 2010, MNRAS, 408, 1969

Vegetti S., Lagattuta D. J., McKean J. P., Auger M. W., Fassnacht C. D., Koopmans, 2012, Nature, 481, 341

Vegetti S., Koopmans L. V. E., Auger M. W., Treu T., Bolton A. S., 2014, MNRAS, 442, 2017

Vogelsberger M. et al., 2014a, MNRAS, 444, 1518

Vogelsberger M. et al., 2014c, Nature, 509, 177

Vogelsberger M. et al., 2018b, MNRAS, 474, 2073

Vogelsberger M., Zavala J., Loeb A., 2012, MNRAS, 423, 3740

Vogelsberger M., Genel S., Sijacki D., Torrey P., Springel V., Hernquist L., 2013, MNRAS, 436, 3031

Vogelsberger M., Zavala J., Simpson C., Jenkins A., 2014b, MNRAS, 444, 3684

Vogelsberger M., Zavala J., Cyr-Racine F.-Y., Pfrommer C., Bringmann T., Sigurdson K., 2016, MNRAS, 460, 1399

Vogelsberger M., Zavala J., Schutz K., Slatyer T. R., 2018a, preprint (arXiv:1805.03203)

Weinberger R. et al., 2017, MNRAS, 465, 3291

Yoshida N., Springel V., White S. D. M., Tormen G., 2000, ApJ, 544, L87

Zavala J., Vogelsberger M., Walker M. G., 2013, MNRAS, 431, L20

This paper has been typeset from a TeX/LaTeX file prepared by the author.